

# Discrete structure of the brain rhythms

L. Perotti<sup>1</sup>, J. DeVito<sup>2</sup>, D. Bessis<sup>1</sup>, Y. Dabaghian<sup>2\*</sup>

<sup>1</sup>*Department of Physics, Texas Southern University,  
3100 Cleburne Ave., Houston, Texas 77004,*

<sup>2</sup>*Department of Neurology,  
The University of Texas Health Science Center at Houston,  
Houston, TX 77030*

*\*e-mail: yuri.a.dabaghian@uth.tmc.edu*

(Dated: June 19, 2018)

Neuronal activity in the brain generates synchronous oscillations of the Local Field Potential (LFP). The traditional analyses of the LFPs are based on decomposing the signal into simpler components, such as sinusoidal harmonics. However, a common drawback of such methods is that the decomposition primitives are usually presumed from the onset, which may bias our understanding of the signal's structure. Here, we introduce an alternative approach that allows an impartial, high resolution, hands-off decomposition of the brain waves into a small number of discrete, frequency-modulated oscillatory processes, which we call oscillons. In particular, we demonstrate that mouse hippocampal LFP contain a single oscillon that occupies the  $\theta$ -frequency band and a couple of  $\gamma$ -oscillons that correspond, respectively, to slow and fast  $\gamma$ -waves. Since the oscillons were identified empirically, they may represent the actual, physical structure of synchronous oscillations in neuronal ensembles, whereas Fourier-defined "brain waves" are nothing but poorly resolved oscillons.

## I. INTRODUCTION

Neurons in the brain are submerged into a rhythmically oscillating electrical field, created by synchronized synaptic currents [1]. The corresponding potential, known as local field potential (LFP) is one of the principal determinants of neural activity at all levels, from the synchronized spiking of the individual neurons to high-level cognitive processes [2]. The attempts to understand the structure and function of LFP oscillations, and of their spatiotemporally smoothed counterparts—the electroencephalograms (EEG), continues for almost a century and a systematic understanding of their roles begins to shape.

The possibility to identify true physiological functions of the LFP depends fundamentally on the mathematical and computational tools used for its analysis. The majority of the currently existing methods are based on breaking the signal into a combination of simpler components, such as sinusoidal harmonics or wavelets [3, 4], and then correlating them with physiological, behavioral and cognitive phenomena [5, 6]. For example, wavelet analysis is most appropriate for studying time-localized events, such as ripples or spindles [7, 8], whereas for the general analyses, the oscillatory nature of LFPs suggests using Fourier decomposition into a set of plane waves with a fixed set of frequencies  $\omega, 2\omega, 3\omega, \dots$ . The latter approach has dominated the field for the last several decades and now constitutes, in effect, the only systematic framework for our understanding of the structure and the physiological functions of the brain rhythms [6]. However, a common flaw of these methods is that the decomposition primitives are presumed from the onset, and the goal of subsequent analyses reduces merely to identifying the combination that best reproduces the original signal. Since no method can guarantee a universally good representation of

the signals’ features and since the physiological structure of the LFPs remains unknown, obtaining a physically adequate description of the brain rhythms is a matter of fundamental importance.

Below we propose a novel approach of LFP analysis based on a recent series of publications [9–11], in which an optimal set of frequencies  $\omega_1, \omega_2, \dots$ , is estimated, at every moment of time  $t$ , using the Padé Approximation Theory [12]. In contrast with the Fourier method, these adaptively optimized values can freely change within the sampling frequency domain, guided only by the signal’s structure. The resulting harmonics are highly responsive to the signals’ dynamics and capture subtle details of the signal’s spectrum very effectively, as one would expect from a Padé Approximation based technique. We call the new method Discrete Padé Transform (DPT), to emphasize certain key correspondences with the traditional Discrete Fourier Transform (DFT).

Applying DPT analyses to LFP rhythms recorded in mouse hippocampi reveals a new level in their structure—a small number of frequency-modulated oscillatory processes, which we call *oscillons*. Importantly, oscillons are observed in the physiologically important theta ( $\theta$ ) [16–18] and gamma ( $\gamma$ ) [19, 20] frequency domains, but are much sharper defined. For example, in the Fourier approach, the  $\theta$ -rhythm is loosely defined as a combination of the plane waves with frequencies between 4 and 12 Hz [16–18]. In contrast, our method suggests that there exists a *single* frequency-modulated wave—the  $\theta$ -oscillon—that occupies the entire  $\theta$  frequency band and *constitutes* the  $\theta$ -rhythm. Similarly, we observe oscillons in the low and high  $\gamma$ -frequency domains. The superposition of the oscillons reproduces the original LFP signal with high accuracy, which implies that these waves provide a remarkably sparse representation of the LFP oscillations. Since oscillons emerged as a result of empirical analyses, we hypothesize that they represent the actual, physical structure of synchronized neuronal oscillations, which were previously approximately described as the Fourier-defined “brain waves.”

## II. RESULTS

**The oscillons.** We implemented a “Short Time Padé Transform” (STPT), in which a short segment of the time series (that fits into a window of a width  $T_w$ ) is analyzed at a time. This allows us to follow the signal’s spectral composition on moment-to-moment basis and to illustrate its spectral dynamics using Padé spectrograms (the analogues of to the standard Fourier spectrograms [13, 14]).

Applying these analyses to the hippocampal LFPs recorded in awake rodents during habituation stage [15], we observed that there exist two types of time-modulated frequencies (Fig. 1). First, there is a set of frequencies that change across time in a regular manner, leaving distinct, continuous traces—the *spectral waves*. As shown on Fig. 1A, the most robust, continuous spectral waves with high amplitudes (typically three or four of them) are confined to the low frequency domain and roughly correspond to the traditional  $\theta$ - and  $\gamma$ -waves [16, 19]. The higher frequency (over 100 Hz) spectral waves are scarce and short, representing time-localized oscillatory phenomena that correspond, in the standard Fourier approach, to fast  $\gamma$  events [21], sharp wave ripples (SWRs) [22] or spindles [23]. Second, there exists a large set of “irregular” frequencies that assume sporadic values from one moment to another, without producing contiguous patterns and that correspond to instantaneous waves with very low amplitudes.

From the mathematical perspective, the existence of these two types of instantaneous frequencies can be explained based on several subtle theorems of Complex Analysis, which point out that the “irregular” harmonics represent the signal’s noise component, whereas the “regular,” stable harmonics define its oscillatory part (see [24–27] and the Mathematical Supplement). Thus, in addition to revealing subtle dynamics the frequency spectrum, the DPT method allows a context-

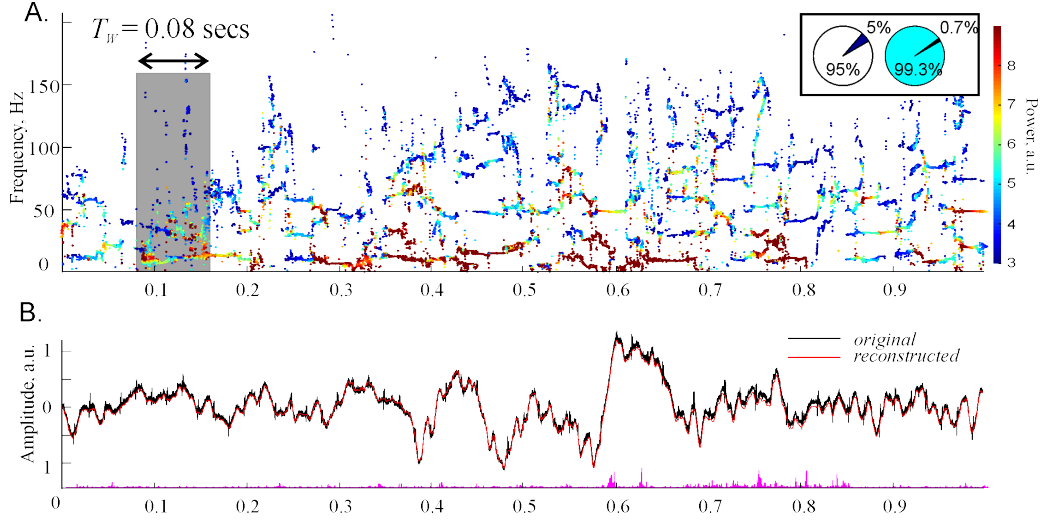


**Figure 1: Padé spectrograms of the hippocampal LFP signal.** **A.** Discrete Padé Spectrogram (DPS) produced for the LFP signal recorded in the CA1 region of the rodent hippocampus at the sampling rate 10 kHz. At each moment of time, the vertical cross section of the spectrogram gives the instantaneous set of the regular frequencies. At consecutive sequence of moments of time, these frequencies produce distinct, contiguous traces, which can be regarded as timelines of discrete oscillatory processes—the spectral waves with varying frequencies  $\omega_q(t)$ , amplitudes  $A_q(t)$  (shown by the color of dots) and phases  $\psi_q(t)$  (not shown). Note that the higher frequency spectral waves tend to have lower amplitudes. Highest amplitudes appear in the  $\theta$ -region, i.e. in the frequency range between 4 and 12 Hz. The spectral waves above 100 Hz tend to be scarce and discontinuous, representing time-localized splashes of LFP. The width of the time window is  $T_W = 0.08$  sec (800 data points). The pie diagrams in the box show that stable harmonics constitute only 5% of their total number, but carry over 99% of the signal’s power. **B.** The LFP signal reconstructed from the regular poles (red trace) closely matches the original signal (black trace) over its entire length, which demonstrates that the oscillon decomposition (2) provides an accurate representation of the signal. The difference between the original and the reconstructed signal is due to the removed noise component—the discarded “irregular” harmonics (the magenta “grass” along the  $x$ -axis). Although their number is large (about 90 – 99% of the total number of frequencies), their combined contribution is small—only about  $10^{-3} - 10^{-4}$  of the signals power.

free, impartial identification of noise, which makes it particularly important for the biological applications [28, 29].

As it turns out, the unstable, or “noisy,” frequencies typically constitute over 95% of the total number of harmonics (Fig. 1A). However, the superposition of the harmonics that correspond to the remaining, *stable* frequencies captures the shape of the signal remarkably well (Fig. 1B). In other words, although only a small portion of frequencies are regular, they contribute over 99% of the signal’s amplitude: typically, the original LFP signal differs from the superposition of the stable harmonics by less than 1%. If the contribution of the “irregular” harmonics (i.e., the noise component  $\xi(t)$ ) is included, the difference is less than  $10^{-4} - 10^{-6}$  of the signal’s amplitude.

These results suggest that the familiar Fourier decomposition of the LFP signals into a superposition of plane waves with *constant* frequencies,

$$r(t) = \sum_{p=1}^N a_p e^{i\omega_p t}, \quad (1)$$

should be replaced by a combination of a few phase-modulated waves embedded into a weak noise background  $\xi(t)$ ,

$$s(t) = \sum_{q=1}^M A_q e^{i\phi_q(t)} + \xi(t), \quad (2)$$

which we call *oscillons*. We emphasize that the number  $M \ll N$  of the oscillons in the decomposition (2), their amplitudes  $A_q$ , their phases  $\phi_q$  and the time-dependent frequencies  $\omega_q(t) = \partial_t \phi_q(t)$  (i.e., the spectral waves shown on Fig. 1A) are reconstructed on moment-by-moment basis from the local segments of the LFP signal in a hands-off manner: we do not presume *a priori* how many frequencies will be qualified as “stable,” when these stable frequencies will appear or disappear, or how their values will evolve in time, or what the corresponding amplitudes will be. Thus, the structure of the decomposition (2) is obtained *empirically*, which suggests that the oscillons may reflect the actual, physical structure of the LFP rhythms.

**The spectral waves.** We studied the structure the two lowest spectral waves using high temporal resolution spectrograms (Fig. 2A). Notice that these spectral waves have a clear oscillatory structure,

$$\omega_q(t) = \omega_{q,0} + \omega_{q,1} \sin(\Omega_{q,1}t + \varphi_{q,1}) + \omega_{q,2} \sin(\Omega_{q,2}t + \varphi_{q,2}) + \dots, \quad q = 1, 2, \quad (3)$$

characterized by a mean frequency  $\omega_{q,0}$ , as well as by the amplitudes,  $\omega_{q,i}$ , the frequencies,  $\Omega_{\theta,i}$ , and the phases,  $\varphi_{\theta,i}$ , of the modulating harmonics. The lowest wave has the mean frequency of about 8 Hz and lies in the domain  $2 \leq \omega/2\pi \leq 17$  Hz, which corresponds to the  $\theta$ -frequency range [16]. The second wave has the mean frequency of about 35 Hz and lies in the low- $\gamma$  domain  $25 \leq \omega/2\pi \leq 45$  Hz [19]. Importantly, the spectral waves are well separated from one another: the difference between their mean frequencies is larger than their amplitudes, which allows indexing them using the standard brain wave notations, as  $\omega_\theta(t)$  and  $\omega_\gamma(t)$  respectively, e.g.,

$$\omega_\theta(t) = \omega_{\theta,0} + \omega_{\theta,1} \sin(\Omega_{\theta,1}t + \varphi_{\theta,1}) + \omega_{\theta,2} \sin(\Omega_{\theta,2}t + \varphi_{\theta,2}) + \dots, \quad (4)$$

for the  $\theta$  spectral wave an

$$\omega_\gamma(t) = \omega_{\gamma,0} + \omega_{\gamma,1} \sin(\Omega_{\gamma,1}t + \varphi_{\gamma,1}) + \omega_{\gamma,2} \sin(\Omega_{\gamma,2}t + \varphi_{\gamma,2}) + \dots \quad (5)$$

for the low- $\gamma$  spectral wave, etc.

We verified that these structures are stable with respect to the variations of the SDPT parameters, e.g., to changing the sliding window size,  $T_W$ . The size of the sliding window, and hence the number of points  $N$  that fall within this window can be changed by over 400%, without affecting the overall shape of the spectral waves (Fig. 2B). The smallest window size (a few milliseconds) is restricted by the requirement that the number of data points captured within  $T_W$  should be bigger than the physical number of the spectral waves. On the other hand, as the maximal value of  $T_W$  is limited by the temporal resolution of STPT: if the size of the window becomes comparable to the characteristic period of a physical spectral wave, then the reconstructed wave loses its undulating shape and may instead produce a set of sidebands surrounding the mean frequency [3]. This effect limits the magnitude of the  $T_W$  to about 50 milliseconds—for larger values of  $T_W$ , the undulating structure begins to straighten out, as shown on Fig. 1A for  $T_W = 80$  msec.

In contrast with this behavior, the values of the irregular frequencies are highly sensitive to the sliding window size and other DPT parameters, as one would expect from a noise-representing component. The corresponding “noisy” harmonics can therefore be easily detected and removed using simple numerical procedures (see Mathematical Supplement). Moreover, we verified that the structure of the Padé Spectrogram, i.e., of the parameters the oscillons remain stable even if the amount of numerically injected noise exceeds the signal’s natural noise level by an order of magnitude (about  $10^{-4}$  of the signal’s mean amplitude), which indicates that the oscillatory part of the signal is robustly identified.

**Parameters of the low frequency oscillons.** To obtain a more stable description of the underlying patterns, we interpolated the spectral waves over the uniformly spaced time points (Fig. 3A)

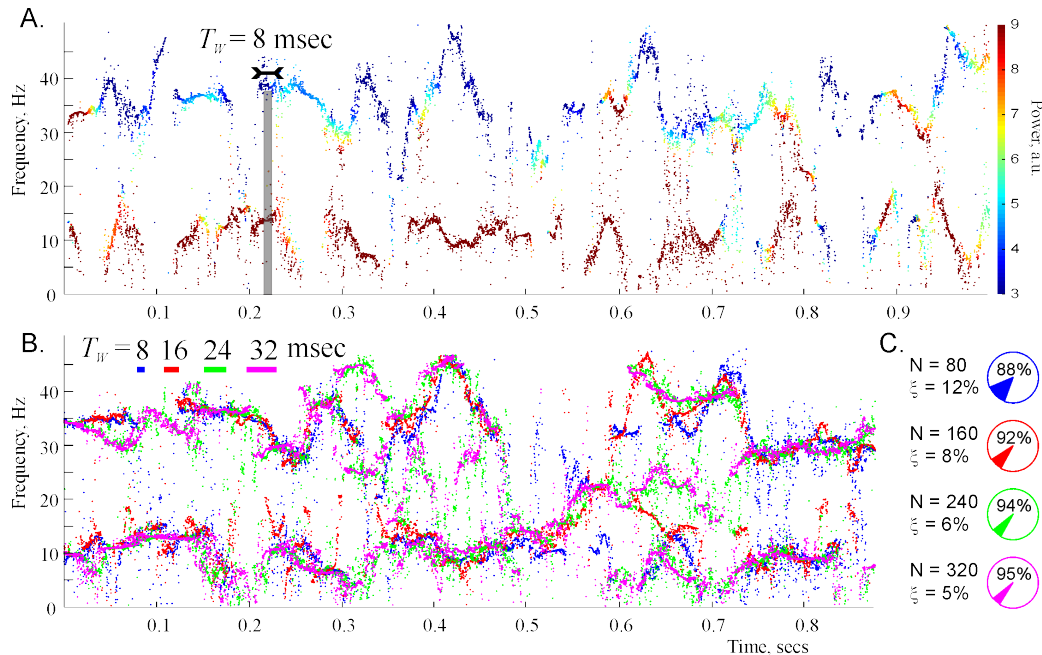


Figure 2: **Padé spectrograms of the rat hippocampal LFP signal.** **A.** A detailed representation of the lower portion the spectrogram recomputed for  $T_W = 0.08$  sec (80 data points) exhibits clear oscillatory patterns. **B.** The shape of the two lowest frequency spectral waves is stable with respect to the variation of time window size,  $T_W$ . The strikes of different color in the top left corner represent the widths of the four  $T_W$ -values used in DPT analysis. The corresponding reconstructed frequencies are shown by the dots of the same color. Although the frequencies obtained for different  $T_W$ s do not match each other exactly, they outline approximately the same shape, which, we hypothesize, reflects the physical pattern of synchronized neuronal activity that produced the analyzed LFP signal. **C.** Pie diagrams illustrate the numbers of data points  $N = 80$ ,  $N = 160$ ,  $N = 240$ ,  $N = 320$  and the mean numbers of the regular and the irregular (noisy) harmonics in each case.

and then studied the resulting “smoothened” spectral waves using the standard DFT tools. In particular, we found that, for studied LFP signals, the mean frequency of the  $\theta$ -oscillon is about  $\omega_{\theta,0}/2\pi = 7.5 \pm 0.5$  Hz and the mean frequency of the low  $\gamma$ -oscillon is  $\omega_{\gamma,0}/2\pi = 34 \pm 2$  Hz, which correspond to the traditional (Fourier defined) average frequencies of the  $\theta$  and the low  $\gamma$  rhythms.

The amplitudes of the  $\theta$  and the low  $\gamma$  spectral waves— $7.0 \pm 1.5$  Hz and  $10.1 \pm 1.7$  Hz respectively—define the frequency domains (spectral widths) of the  $\theta$  and the low  $\gamma$  rhythms (Fig. 3B). The amplitudes of the corresponding oscillons constitute approximately  $A_\theta/A \approx 62\%$  and  $A_{\gamma_1}/A \approx 17\%$  of the net signals’ amplitude  $A$ , i.e., the  $\theta$  and the low  $\gamma$  oscillons carry about 80% of the signals’ magnitude.

The oscillatory parts of the spectral waves are also characterized by a stable set of frequencies and amplitudes: for the first two modulating harmonics we found  $\omega_{\theta,1}/2\pi \approx 4.3$  Hz,  $\omega_{\theta,2}/2\pi \approx 3.2$  Hz for the  $\theta$  spectral wave (4) and  $\omega_{\gamma,1}/2\pi \approx 6.1$  Hz,  $\omega_{\gamma,2}/2\pi \approx 4.3$  Hz for the  $\gamma$  spectral wave (14). The corresponding modulating frequencies for the  $\theta$ -oscillon are  $\Omega_{\theta,1} = 4.3 \pm 0.45$  Hz,  $\Omega_{\theta,2} = 7.3 \pm 0.48$  Hz,  $\dots$ , (Fig. 3C). The lowest modulating frequencies for the  $\gamma$ -oscillon are slightly higher:  $\Omega_{\gamma,1} = 5.3 \pm 0.41$  Hz,  $\Omega_{\gamma,2} = 8.3 \pm 0.51$  Hz,  $\dots$ . In general, the modulating frequencies tend to increase with the mean frequency.

Importantly, the reconstructed frequencies sometimes exhibit approximate resonance relationships (Fig. 3C), implying that some of the higher order frequencies may be overtones of a smaller

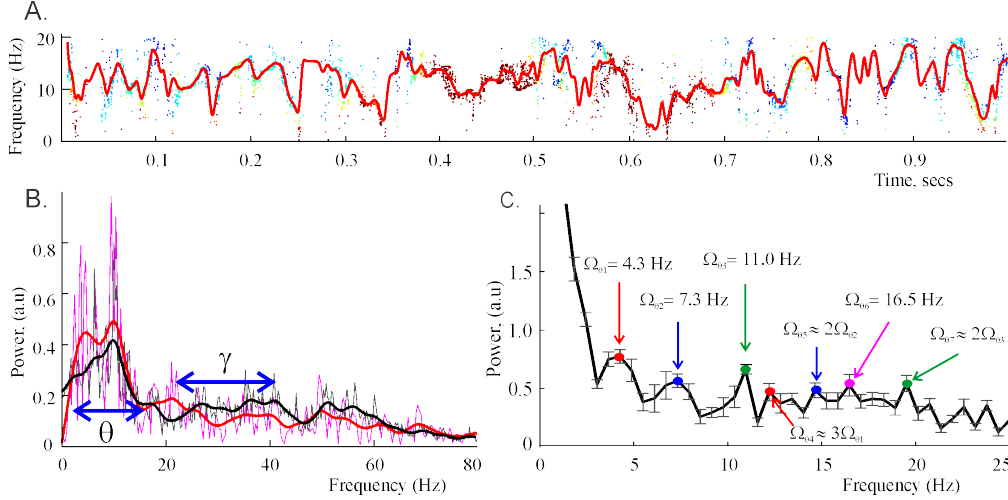


**Figure 3: Parameters of the spectral waves.** **A.** The red curve shows the smoothed  $\theta$  spectral wave, obtained by interpolating the “raw” trace of the reconstructed frequencies shown on Fig. 2A over the uniformly spaced time points. **B.** The power spectra produced by the Discrete Padé decomposition (DPT, red) and the standard Discrete Fourier decomposition (DFT, black) exhibit characteristic peaks around the mean frequency of the  $\theta$ -oscillation,  $\omega_{\theta,0}/2\pi \approx 7.5$  Hz. The height of the peaks defines the amplitudes, respectively, of the  $\theta$ -oscillation in the DPT approach and of the  $\theta$ -rhythm in DFT. A smaller peak at about 34 Hz corresponds to the mean frequency of the low  $\gamma$  oscillation,  $\omega_{\gamma,0}/2\pi \approx 34$ . The  $\theta$  and the low  $\gamma$  frequency domains, marked by blue arrows, are defined by the amplitudes of the corresponding spectral waves. **C.** The smoothed waves are used to compute the DFT transform and to extract the modulating frequencies  $\Omega_{\theta,1} \approx 4.3$  Hz,  $\Omega_{\theta,2} \approx 7.3$  Hz,  $\Omega_{\theta,3} \approx 11$  Hz, ..., of the decomposition (4–14). The error margin in most estimates is  $\pm 0.5$  Hz. Notice that there exist several approximate resonant relationships, e.g.,  $\Omega_{\theta,4} \approx 3\Omega_{\theta,1}$ ,  $\Omega_{\theta,5} \approx 2\Omega_{\theta,2}$  and  $\Omega_{\theta,7} \approx \Omega_{\theta,3}$ , which suggest that the spectral  $\theta$ -wave contains higher harmonics of a smaller set of prime frequencies.

set of prime frequencies that define the dynamics of neuronal synchronization [37–39].

### III. DISCUSSION

The Fourier and the Padé decompositions agree in simple cases, e.g., both spectrograms resolve the individual piano notes in a 10 sec excerpt from one of Claude Debussy’s Preludes (Fig. 4).

However, in more complex cases the DTP approach produces a more accurate description of the signal’s structure. For example, the Padé decomposition previously used to detect faint gravitational waves in resonant interferometers, which were completely missed by the Fourier analyses [30]. In the case of the LFP signals, this method identifies a small number of structurally stable, frequency-modulated oscillons which may reflect the physical synchronization patterns in the hippocampal network.

Why these structures were not previously observed via Fourier method? The reason lies in the insufficient resolution of the latter, which is due to the well-known inherent conflict between the frequency and the temporal resolutions in Fourier Analysis [32]. Indeed, in order to observe changes in the signal’ spectrum, the size of the sliding time window,  $T_W$ , should be *smaller* than the characteristic timescale of frequency’s change,  $T_W < \Delta T$ . On the other hand, reducing  $T_W$  implies lowering the number of data points in the sliding window, which results in an equal reduction of the number of the discrete harmonics, in both the DFT and the DPT approaches. However, since in

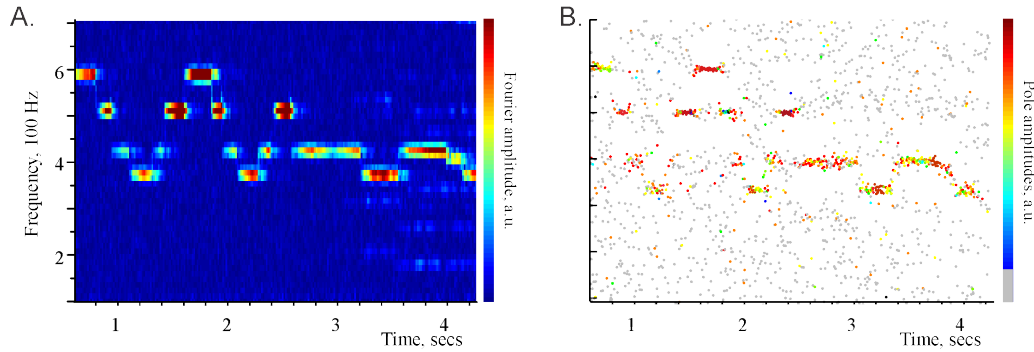


Figure 4: **Correspondence between the Discrete Fourier (left) and Padé (right) spectral decompositions.** **A.** Fourier spectrogram of a 10 second long excerpt from C. Debussy’s Preludes, Book 1: No. 8. *La fille aux cheveux de lin*, in which the individual notes are clearly audible. The high amplitude streaks (colorbar on the right) correspond to the notes (D#5, B4, G4, F4, G4, B4, D5, B4, G4, F4, G4, B4, G4, F4, G4, F4, ...). **B.** The Discrete Padé spectrogram of the same signal. The frequencies produced by large amplitude poles (see colorbar on the right) match the frequencies of their Fourier counterparts shown on the left. The frequencies produced the Froissart doubles form a very low amplitude background “dust,” shown in gray. Our main hypothesis is that the oscillons detected in the LFP signals by the DPT method may be viewed as “notes” within the neuronal oscillations.

DFT method these harmonics are restricted to a rigid, uniformly distributed set of values (Fig. 5A), a decrease in the number of data points necessarily results in an increase of the interval between neighboring discrete frequencies, i.e., in an unavoidable reduction of frequency resolution. In contrast, the DPT harmonics can move freely in the available frequency domain, responding to the spectral structure of the signal and providing a high resolution of the signals’ spectrum [11]. In other words, an increase in temporal resolution in DPT does not necessarily compromise the frequency resolution and vice versa, which allows describing the signal dynamics much more capably.

In the specific case illustrated on Fig. 2, the characteristic amplitudes of the spectral waves is about 15 – 25 Hz. Producing such frequency resolution in DFT at the sampling rate  $S = 10$  kHz would require some  $N = 300 - 500$  constant frequency harmonics, i.e.,  $N = 300 - 500$  data points, which can be collected over  $T_W = 30 - 50$  msec time window. However, the characteristic period of the spectral waves is about 60 msec, which implies that for such  $T_W$ s, the DFT will not be able to resolve the frequency wave dynamics and will replace it by an average frequency with some sidebands (see Mathematical Supplement). In contrast, a DPT that uses as few as 80 data points in a  $T_W = 8$  msec wide time window, reliably capturing the shape of the spectral wave, which then remains overall unchanged as  $T_W$  increases fourfold.

Another key property of the DPT method is the intrinsic marker of noise, which is particularly important in biological applications [28, 29]. In general, the task of distinguishing “genuine noise” from a “regular, but highly complex” signal poses not only a computational, but also a profound conceptual challenge [33, 34]. In contrast with the standard *ad hoc* approaches, the DPT method allows a context-free, impartial identification of the noise component, as the part of the signal represented by the irregular harmonics.

The new structure also dovetails with the theoretical views on the origins of the LFP oscillations as on a result of synchronization of the neuronal spiking activity in both the excitatory and inhibitory networks [37–39]. Broadly speaking, it is believed that the LFP rhythms are due to a coupling between the electromagnetic fields produced by local neuronal groups [1]. If the coupling between these groups is sufficiently high, then the individual fields oscillating with amplitudes  $a_p$



and phases  $x_p$  synchronize, yielding a nonzero mean field  $\sum_p a_p e^{ix_p} = A e^{i\phi}$  that is macroscopically observed as LFP [37–39]. In particular, the celebrated Kuramoto Model [37] describes the synchronization between oscillators via a system of equations

$$\partial_t x_q = \omega_{q,0} + K \sum_p \sin(x_q - x_p), \quad (6)$$

according to which the oscillators transit to a synchronized state, as the coupling strength  $K$  increases. The Eqs. (6) directly point out that the synchronized frequency,  $\omega(t) = \partial_t \phi$ , should have the form (3). However, this form of expansion has not been previously extracted from the experimental data, which may be due to the fact that the Fourier method does not resolve the spectral structure in sufficient detail (Fig. 6). In contrast, the description of the LFP oscillations produced by the DPT method may provide such resolution and help to link the empirical data to theoretical models of neuronal synchronization.

#### IV. MATHEMATICAL SUPPLEMENT

**The Discrete Fourier Transform (DFT)** is used to represent a given time series as a superposition of discrete harmonics with *fixed* frequencies (Fig. 5A). To that end,  $N$  recorded values,  $s_1, s_2, \dots, s_N$ , are convolved with a set of  $N$  discrete harmonics,  $z_l = e^{i2\pi l/N}$ ,

$$A_l = \sum_n s_n z_l^n. \quad (7)$$

The magnitude of this convolution defines the amplitude of the discrete plane wave  $z_l$  in the discrete Fourier decomposition: the most prominent oscillatory components produce peaks in the Fourier transform, whereas the noise broadens these peaks, lowers their magnitudes and generally obscures the spectral properties of the signal [32]. Similar effects are produced by the signal's nonstationarity, i.e., by the time dependence of the signal's frequencies.

**The Discrete Padé Transform (DPT)** method discussed here is based on studying the so-called  $z$ -transform of the recorded time series,

$$S(z) = \sum_n s_n z^n, \quad (8)$$

where  $z = x + iy$  is a complex variable (i.e., the series expansion (8) is an extension of (7) into the entire complex plane), and of its Padé approximant—a ratio of two polynomials  $P_{N-1}(z)$  and  $Q_N(z)$ ,

$$S_N(z) = P_{N-1}(z)/Q_N(z) \quad (9)$$

that approximates  $S(z)$  to the  $2N$ -th order of  $z$  [12].

*Oscillatory component.* In the analyses of the oscillatory signals, the  $N$  roots  $z_p$ ,  $p = 1, \dots, N$ , of the polynomial  $Q_N(z)$ —the poles of the Padé approximant—play the role of the discrete Fourier harmonics,  $z_l$ , in the DFT: they capture the spectral structure of the signal [9–11]. Indeed, consider a signal  $r(t)$  obtained as a superposition of  $N_p$  damped oscillators,

$$r(t) = \sum_p A_p e^{-\alpha_p t} \cos(\omega_p t + \varphi_p), \quad (10)$$

where  $A_p$  is the amplitude of the  $p$ th oscillator with a damping exponent  $\alpha_p$ , frequency  $\omega_p$  and phase  $\varphi_p$ . If the signal is sampled at a frequency  $S$ , then it generates a discrete time series,

$$r_k = \sum_{p=1}^{N_p} c_p e^{i\omega_p^{(+)} k/S} + c_p^* e^{i\omega_p^{(-)} k/S}, \quad k \in \mathbb{Z}, \quad (11)$$



where  $\omega^{(\pm)} = i\alpha_p \pm \omega_p$  and  $c_p = A_p e^{i\varphi_p/2}$ . The generating function of this series,

$$R(z) = \sum_{k=1}^{\infty} r_k z^k = \sum_{p=1}^{N_p} \left( \frac{c_p}{1 - z e^{i\omega_p^{(+)} / S}} + \frac{c_p^*}{1 - z e^{i\omega_p^{(-)} / S}} \right), \quad (12)$$

is a rational fraction of degree  $(2N_p - 1)/2N_p$  with poles

$$z_p^{(\pm)} = e^{-i\omega_p^{(\pm)} / S}.$$

The phase of each pole  $z_p$  defines the frequency  $\omega_p$ , and its magnitude defines the damping constant  $\alpha_p$ . The residue of  $z_p$  defines the amplitude  $A_p$  and the phase  $\varphi_p$  of the corresponding oscillator. Notice that poles come in complex conjugate pairs and have to lie either outside of the unit circle, if the signal is damped ( $\Im\omega_p = \alpha_p > 0$ ), or on the circle if the signal has no damping.

*Noise component.* If a signal is perturbed by an additive noise  $\xi(t)$ , then the generating function (9) of the resulting “noisy” time series  $s_n = r_n + \xi_n$  is the sum of the “regular” and the “noisy” part,  $S(z) = R(z) + \Xi(z)$ , where

$$\Xi(z) = \sum_n \xi_n z^n. \quad (13)$$

A remarkable theorem proven by H. Steinhaus [24] establishes that the poles of  $\Xi(z)$  concentrate, with probability 1, at the unit circle (Fig. 5B). In other words, the generating function of a random data series is an analytic function inside the unit disk, possessing a dense set of poles as  $|z|$  approaches 1. Thus, the total generating function of the full signal  $S(z) = R(z) + \Xi(z)$  has a finite number of poles contributed by  $R(z)$  and an infinite number of poles contributed by  $\Xi(z)$ .

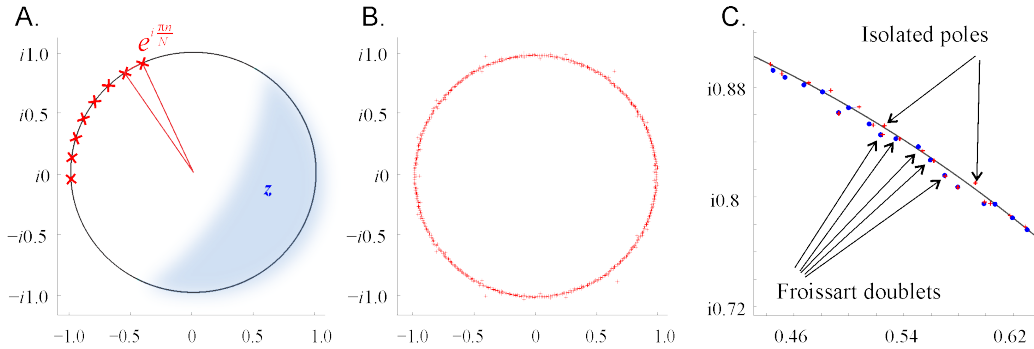


**Figure 5: Fourier and Padé in complex plane.** **A.** The discrete waves,  $z_l = e^{i2\pi l/N}$ , used to construct the Fourier decompositions, are uniformly distributed over the unit circle  $S^1$ , embedded into the complex plane of the variable  $z$ . **B.** The poles of the Padé approximant to the signal’s generating function,  $z_p$  (red crosses), also concentrate in a close vicinity of the unit circle, in accordance with Steinhaus’ theorem [24]. For illustrational purposes, the number of Padé-poles shown on panel B is much larger than the number of harmonics shown on panel A. These poles are not constrained to any *a priori* selected locations; in fact, their positions in the complex plane  $C^1$  are dictated solely by the signal’s structure, which ultimately leads to the super-resolution property [11, 30, 31]. **C.** According to the Froissart’s theory [10, 25], zeros and poles that represent the noise component of the signal form close pairs—the Froissart doublets. A zoom-in into a small segment of the unit circle shows many Froissart doublets (zeros shown as blue dots), and two isolated poles that represent the regular, oscillatory part of the signal.

A key property of the Padé approximant to  $\Xi(z)$  is that its poles occur in close vicinities of its zeros, forming the so-called *Froissart doublets* [25–27] that can be easily detected numerically (Fig. 5C). In our analyses, the typical distance in a pole-zero pair is smaller than  $10^{-6} - 10^{-7}$  in the standard Euclidean metric on  $C^1$ . We hence identified such pairs as the ones smaller than a

critical distance  $\delta = 10^{-5}$ . These results are stable: injecting small amounts of white and colored noise into the signal (about  $10^{-3}$  of the signal's mean amplitude, i.e., at least ten times more than the signal's natural noise level) does not alter the reconstructed positions of the regular poles and hence the parameters the spectral waves remain the same as the “perturbed” Froissart doublets are removed.

***J*-matrix formalism.** In order to obtain a Padé approximation to  $S(z)$  in the entire complex plane, the  $\Xi(z)$  has to be analytically extend through its natural boundary, which remains an open problem of complex analysis. However, the “*J*-matrix approach” developed in a recent series of publications [9–11], allows addressing this problem in practical terms. The generating function  $G(z)$  can be associated with a tri-diagonal Hilbert space operator  $J$  that has  $G(z)$  as its resolvent matrix element,  $G(z) = \langle e_0 | (J - z1)^{-1} | e_0 \rangle$ ,  $e_0 = (1, 0, \dots)$  [12]. In accordance with Steinhaus' theorem, the spectrum of  $J$  consists of two parts: an essential spectrum with support on the unit circle, which represents the noise component and a discrete spectrum, containing a finite number of poles outside the unit circle, which represent the regular component of the signal (a finite number of damped oscillators). In the spectrum of finite order truncations  $J_N$  of the  $J$ -operator, the poles of the Froissart doublets take the place of the essential spectrum. Moreover, these finite matrices can be explicitly constructed as follows. Let us consider the set of subdiagonal Padé approximations to the generating function of a given time series defined by (9). The polynomials  $Q_N(z)$  satisfy a third order recursive relation which can be written in a matrix form,  $J_N V = zV$  where  $J_N$  is the (*tri-diagonal*) *finite order matrix approximation to the J-operator of order N + 1*. The column vector  $V$  is defined by the polynomials  $Q_N$ ,  $V_T = [Q_0(z), Q_1(z), \dots, Q_N(z)]$ . The zeros of  $Q_{N+1}(z)$  define the eigenvalues  $(z_0, z_1, \dots, z_N)$  of  $J_N$  and therefore the poles of  $R_N$ . The same procedure applied to  $P_N$  (with a slightly modified matrix) gives us the zeros of  $G_N$ , thus completely characterizing  $R_N$  itself.

**Short Time Padé Transform, (STPT)** is analogous to the standard Short Time Fourier Transform (STFT) method [13]. Starting with a segment  $s_1, s_2, \dots, s_N$  centered at  $t_1$ , we compute the Padé approximants, identify and discard the Froissart doublets, and then evaluate the frequencies,  $\omega_q(t_1)$ , the amplitudes,  $A_q(t_1)$  and the phases,  $\varphi_q(t_1)$ , associated with the stable poles  $z_1, z_2, \dots, z_{p_1}$ ,  $q = 1, \dots, p_1$ . After that, the window is shifted by  $\Delta T$  to the position centered at  $t_2$ , and the same analysis is applied to the next segment of the time series, revealing the frequencies,  $\omega_i(t_2)$ , the amplitudes,  $A_i(t_2)$  and the phases,  $\varphi_i(t_2)$ ,  $i = 1, \dots, p_2$ , and so on.

**Separating the noise from the oscillations.** The Froissart doublets and the regular poles of  $S(z)$ , exhibit qualitatively different behaviors in response to changes of the DPT algorithms' parameters. If the size of time window  $T_w$  in the STPT is altered, or as it is shifted from one segment of the time series to another, or if the order of the Padé approximant is changed, the Froissart-paired poles move significantly and irregularly around the unit circle, as one would expect from a structure that represents noise. In contrast, the poles associated with the regular part of the signal remain stable and isolated. These differences can be easily detected numerically, producing the computational DPT method [9, 10].

Note that every data point obtained by the STPT method is obtained independently: evaluation of  $N$  frequencies at each time-step, identification of the “noisy” vs. “regular” frequencies, etc. does not affect the values obtained at the other time-steps and hence the pattern formed by the data points is completely empirical.

**Computing the parameters of the spectral waves.** Since the instantaneous parameters of the oscillons are computed independently based on a finite number of data points, the reconstructed spectral waves contain gaps and other irregularities. We therefore construct the smoothed spectral waves by interpolating the “raw” traces of the regular frequencies over the uniformly spaced

time points, and compute the mean parameters  $\omega_{q,0}$ ,  $\omega_{q,i}$ ,  $\Omega_{q,i}$ , and  $\varphi_{q,i}$  in the expansion

$$\omega_q(t) \equiv \partial_t \phi_q = \omega_{q,0} + \omega_{q,1} \sin(\Omega_{q,1}t + \varphi_{q,1}) + \omega_{q,2} \sin(\Omega_{q,2}t + \varphi_{q,2}) + \dots \quad (14)$$

using the standard DFT methods.

The Fig. 6 illustrates how the inherent conflict between the time and the frequency resolutions obscures the spectral waves in the Fourier spectrogram.

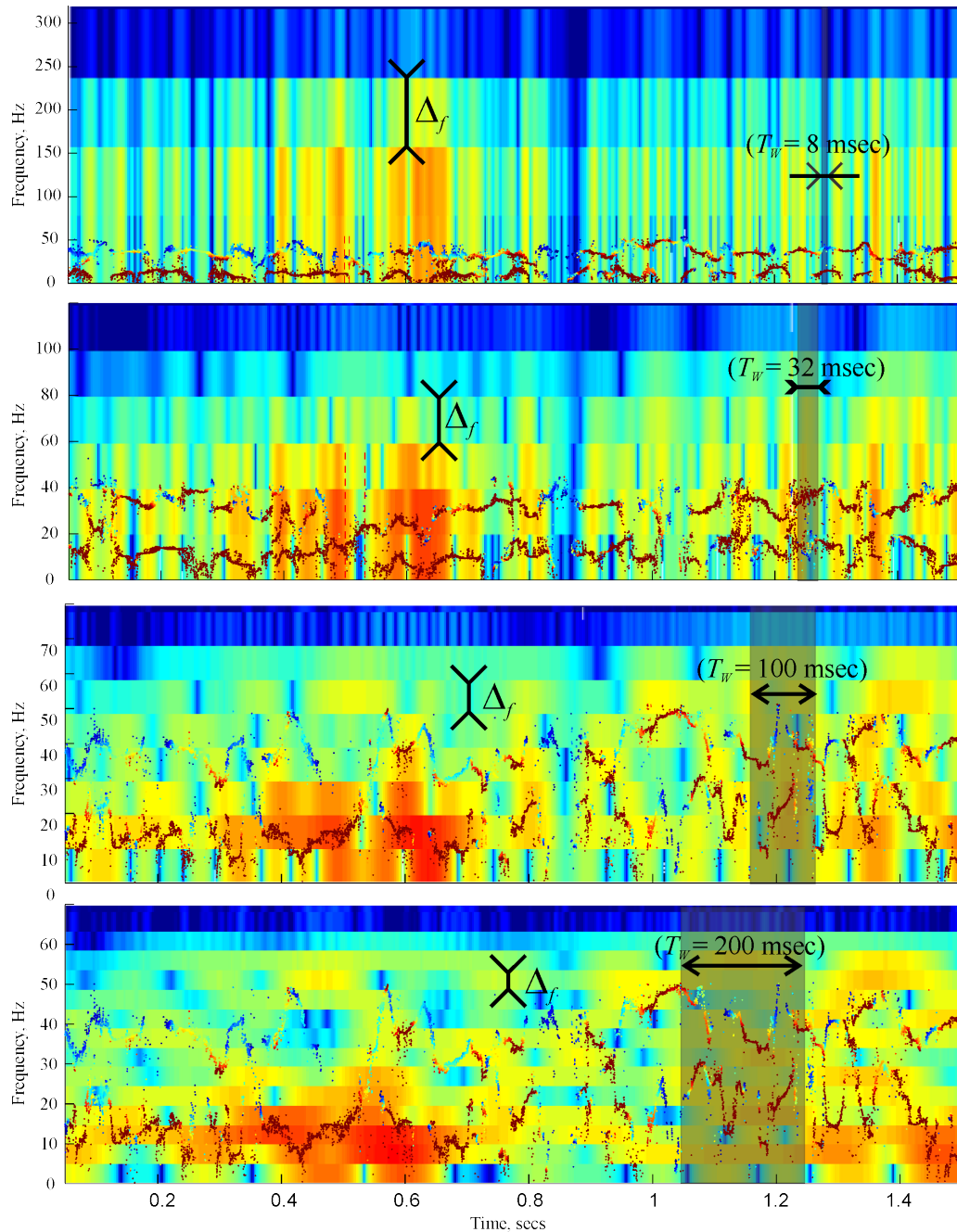


**Figure 6: Insufficiency of Fourier resolution.** The two lowest ( $\theta$  and low- $\gamma$ ) spectral waves of an LFP signal, filtered between 1 and 56 Hz, are superimposed on four Fourier spectrograms of the same signal, computed for  $T_W = 8$  msec,  $T_W = 32$  msec,  $T_W = 100$  msec and  $T_W = 200$  msec. The sliding window widths  $T_W$  are shown by gray vertical stripes. The horizontal stripes on each Fourier spectrogram indicate the magnitude of the spectral resolution,  $\Delta_f$ . The spectral resolution of the Fourier spectrogram becomes comparable to the frequency scale of the spectral waves only for  $T_W = 100$  msec (third panel from the top), but the temporal resolution at this value exceeds the characteristic period of the spectral waves. Increasing the frequency resolution broadens the window size beyond the spectral waves' period (bottom panel) and vice versa, increasing temporal resolution destroys the frequency resolution (top two panels). As a result, the spectral waves remain unresolved by the DFT, which can only detect a band of increased amplitudes, but not the detailed pattern of the oscillating frequencies.

The wavelet spectrograms (scalograms) of the same signal using three different wavelets are shown on Fig. 7.

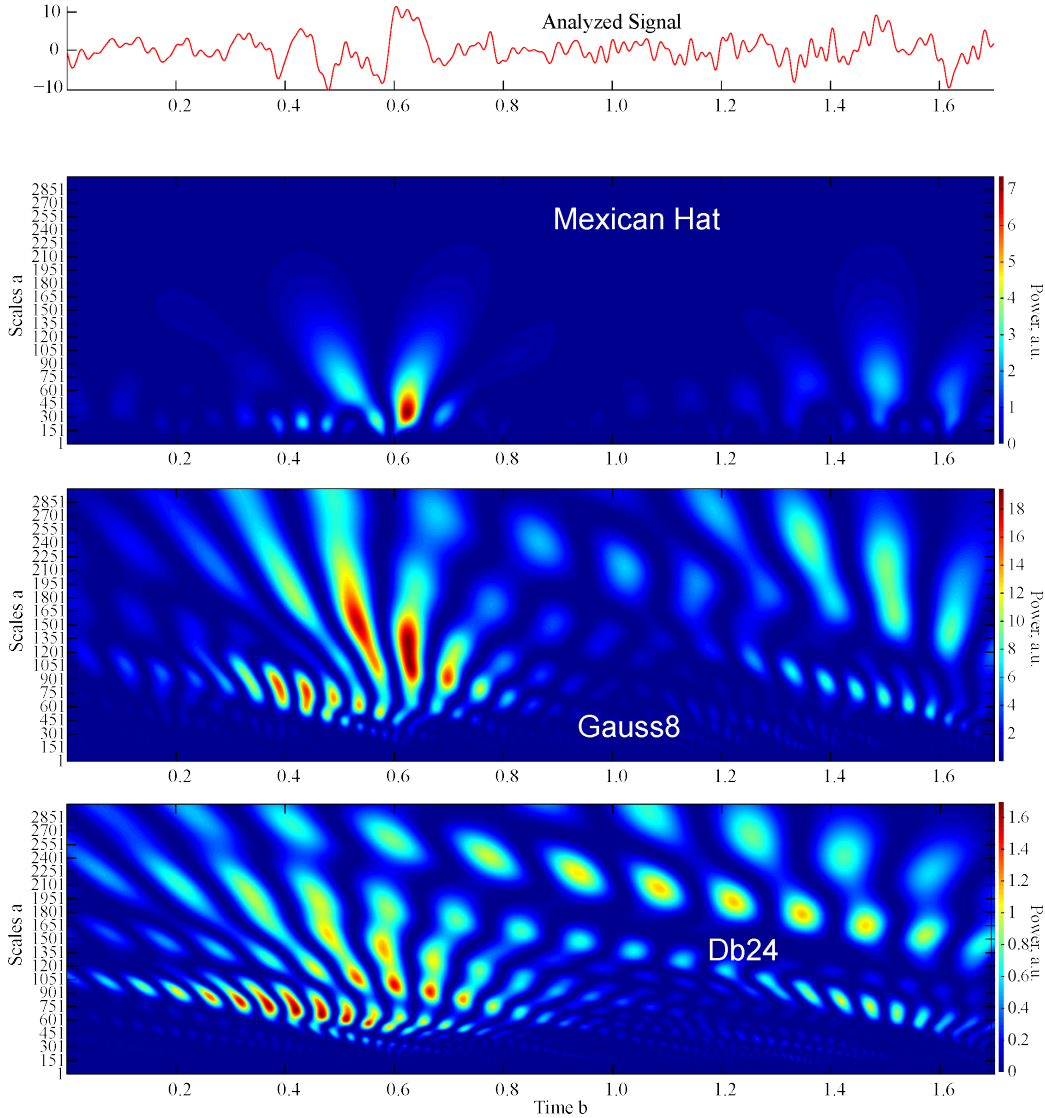


Figure 7: **Wavelet spectrograms** of the same signal, computed for the “Mexican hat” (top panel), the Gauss wavelet of level 8 (middle panel) and Daubechies’ wavelet of level 24 (bottom panel). In all three cases, the maxima of the wavelet coefficients correspond to undulating patterns of the signals’ amplitude at different temporal scales but do not resolve the spectral waves.

To illustrate the effectiveness of the proposed method, we simulated a superposition of five artificial oscillons with the amplitudes  $A_1 = 0.5$ ,  $A_2 = 0.3$ ,  $A_3 = 0.15$ ,  $A_4 = 0.1$  and  $A_5 = 0.05$ , the mean frequencies are  $\omega_{1,0} = 5$  Hz,  $\omega_{2,0} \approx 20$  Hz,  $\omega_{3,0} \approx 30$  Hz,  $\omega_{4,0} \approx 40$  Hz, and  $\omega_{5,0} \approx 50$  Hz, and five modulating frequencies  $\omega_{1,1} = 2$  Hz,  $\omega_{2,1} = 2.5$  Hz,  $\omega_{3,1} = 4$  Hz,  $\omega_{4,1} = 5$  Hz and  $\omega_{5,1} = 6$  Hz respectively. The amplitudes of the frequency modulations are approximately  $\pi$  Hz in all cases. The resulting “spectral waves” are shown as black sinusoids in the background of the four panels of Fig. 8. Each panel corresponds to a particular window width:  $T_W = 0.10$  sec,  $T_W = 0.15$  sec,  $T_W = 0.2$  sec and  $T_W = 0.25$  sec, at the sampling rate of  $S = 1000$  Hz. In the first case, the DPT is therefore based on  $N_1 = 100$  data points per window, i.e., 50 sample frequencies occupying the range between 0 and 500 Hz, or about one frequency per 10 Hz interval. As shown

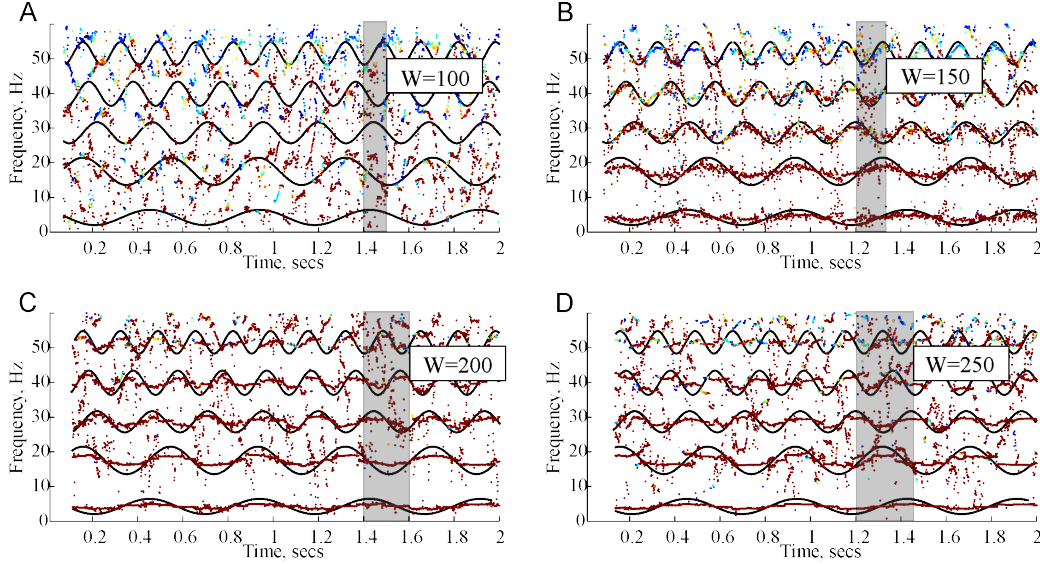


Figure 8: **Discrete Padé spectrograms** of the simulated combination of five oscillons, computed for four window widths ( $T_W = 0.10$  sec,  $T_W = 0.15$  sec,  $T_W = 0.2$  sec and  $T_W = 0.25$ ). While the first window is too narrow to capture the structure of the spectral waves, the second window resolves them. The last two values of  $T_W$  are too large—the undulating pattern of the spectral waves is replaced by the emerging sidebands.

on the Fig. 8A, this (or smaller) values are insufficient for resolving oscillons with magnitude  $\pm\pi$ : the undulatory pattern is not captured. In the second case, each window contains  $N_2 = 150$  points, or one frequency per  $\approx 6.6$  Hz, and the spectral waves become apparent (Fig. 8B). If window becomes bigger,  $N_3 = 200$  points (Fig. 8C) or  $N_4 = 250$  points (Fig. 8D), the temporal resolution suffers: the patterns of all spectral waves become averaged over the window width. As a result the upper spectral waves produce sidebands and the lowest spectral waves the flatten out. We emphasize however, that the original signal can be reconstructed with high precision in all cases; the issue is only whether the spectral can or cannot be resolved.

For comparison, the corresponding Fourier spectrograms and the wavelet scalogram computed using Daubechies' wavelet of level 24 are shown on Fig. 9.

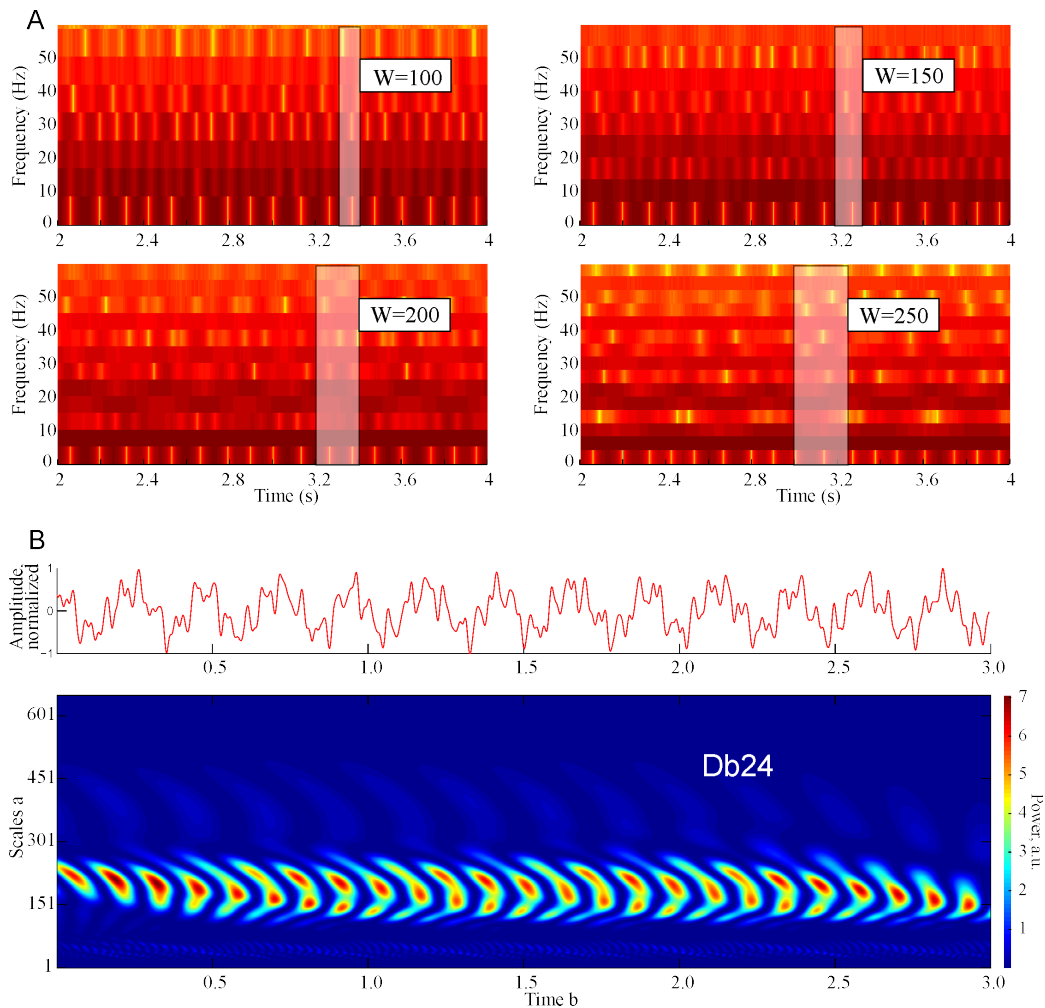


Figure 9: **Alternative methods.** **A.** The Fourier spectrograms of the same signal as shown on Fig. 8, computed for the same window widths ( $T_W = 0.10$  sec,  $T_W = 0.15$  sec,  $T_W = 0.2$  sec and  $T_W = 0.25$ ) do not resolve the simulated spectral waves. **B.** Wavelet spectrograms of the same signal, computed using Daubechies' wavelet of level 24, also captures the undulatory pattern of the signal but does not resolve the spectral waves.



## Acknowledgments

The authors thank Dr. A. Tsvetkov for valuable discussions, Dr. J. Tang from the Baylor College of Medicine for providing LFP signals for this study. The work was supported by the NSF 1422438 grant (Y.D.), by NSF grants 0114796 (2001-2003), DBI-0318415 and DBI-0547695 (2006-2009) (L.P. and D.B.).

## References

- 
- [1] G. Buzsáki, C. Anastassiou, C. Koch (2012), The origin of extracellular fields and currents — EEG, ECoG, LFP and spikes, *Nature Rev. Neurosci.*, 13, 407.
  - [2] G. Thut, C. Miniussi, J. Gross (2012), The Functional Importance of Rhythmic Activity in the Brain, *Current Biology* 22, R658.
  - [3] B. Boashash, Time frequency signal analysis and processing: a comprehensive reference (2003), *Elsevier*, Boston.
  - [4] M. van Vugt, P. Sederberg, M. Kahana (2007), Comparison of spectral analysis methods for characterizing brain oscillations. *J Neurosci Methods*, 162, p. 49.
  - [5] N. Kopell, M. Kramer, P. Malerba, M. Whittington (2010), Are different rhythms good for different functions? *Frontiers in Human Neurosci.*, 4, p. 187.
  - [6] Buzsáki, G (2011), Rhythms in the brain. *Oxford University Press*, USA.
  - [7] F. Battaglia, G. Sutherland, B. McNaughton (2004), Hippocampal sharp wave bursts coincide with neocortical “up-state” transitions. *Learning and Memory* 11, p. 697.
  - [8] E. Sitnikova, A. Hramov, A. Koronovsky, G. van Luijckelaar (2009), Sleep spindles and spike-wave discharges in EEG: Their generic features, similarities and distinctions disclosed with Fourier transform and continuous wavelet analysis. *J. Neurosci. Methods* 180, p. 304.
  - [9] D. Bessis (1996), Padé approximations in noise filtering. *J. Comput. Appl. Math.*, 66, p. 85.
  - [10] D. Bessis, L. Perotti (2009), Universal analytic properties of noise: introducing the J-matrix formalism. *J. of Physics A* 42(36), p. 365202.
  - [11] L. Perotti, D. Vranceanu, D. Bessis (2013), Enhanced Frequency Resolution in Data Analysis. *Amer. J. Comput. Math* 3, p. 242.
  - [12] Baker G., Graves-Morris, P. (1996), Padé Approximants. *Cambridge Univ. Press*.
  - [13] E. Jacobsen, R. Lyons (2003), The sliding DFT. *Signal Processing Magazine. IEEE* 20, p. 74.
  - [14] K. Howell (2001), Principles of Fourier Analysis. *CRC Press*.
  - [15] J. Tang, J. Dani (2009), Dopamine Enables In Vivo Synaptic Plasticity Associated with the Addictive Drug Nicotine. *Neuron* 63: pp. 673-682.
  - [16] G. Buzsáki (2002), Theta oscillations in the hippocampus. *Neuron* 33, pp. 325-40.
  - [17] G. Buzsáki (2005), Theta rhythm of navigation: link between path integration and landmark navigation, episodic and semantic memory. *Hippocampus* 15, pp. 827-840.
  - [18] M. Arai, V. Brandt, Y. Dabaghian (2014), The Effects of Theta Precession on Spatial Learning and Simplicial Complex Dynamics in a Topological Model of the Hippocampal Spatial Map. *PLoS Comput Biol* 10: e1003651.
  - [19] L. Colgin and E. Moser, (2010), Gamma oscillations in the hippocampus. *Physiology* 25, pp. 319-329.

- [20] E. Basso, M. Arai, Y. Dabaghian (2016), Gamma Synchronization Influences Map Formation Time in a Topological Model of Spatial Learning. *PLoS Comput Biol* 12: e1005114.
- [21] D. Sullivan, J. Csicsvari, K. Mizuseki, S. Montgomery, K. Diba, et al. (2011), Relationships between Hippocampal Sharp Waves, Ripples, and Fast Gamma Oscillation: Influence of Dentate and Entorhinal Cortical Activity. *J Neurosci.*, 31 pp. 8605-8616.
- [22] J. Csicsvari and D. Dupret (2014), Sharp wave/ripple network oscillations and learning-associated hippocampal maps. *Philosophical Transactions of the Royal Society B*, 369(1635):20120528.
- [23] C-FV. Latchoumane, H-VV Ngo, J. Born, H-S. Shin (2017), Thalamic Spindles Promote Memory Formation during Sleep through Triple Phase-Locking of Cortical, Thalamic, and Hippocampal Rhythms. *Neuron* 95: p. 424-435.e426.
- [24] H. Steinhaus (1929), Über die Wahrscheinlichkeit dafür dass der Konvergenzkreis einer Potenzreihe ihre natürliche Grenze ist. *Mathematische Zeitschrift* 31, pp. 408-416.
- [25] M. Froissart (1969), Approximation de Padé: application la physique des particules élémentaires. *CNRS RCP Programme n. 29*, p. 1.
- [26] J. Gilewicz, M. Pindor (1997), Padé approximants and noise: A case of geometric series. *J. Comput. Appl. Math* 87, p. 199.
- [27] J. Gilewicz, Y. Kryakin (2003), Froissart doublets in Padé approximation in the case of polynomial noise. *J. Comput. Appl. Math* 153, p. 235.
- [28] A. Faisal, L. Selen, D. Wolpert (2008), Noise in the nervous system. *Nature Rev. Neurosci.* 9, p. 292.
- [29] G. Ermentrout, R. Galán, N. Urban (2008), Reliability, synchrony and noise. *Trends in neurosciences*, 31, p. 428.
- [30] L. Perotti, T. Regimbau, D. Vrinceanu, D. Bessis (2014), Identification of gravitational-wave bursts in high noise using Padé filtering. *Phys. Rev. D*, 90, p. 124047.
- [31] L. Perotti and M. Wojtylak (2018), Matrix methods for Padé approximation: Numerical calculation of poles, zeros and residues. *Linear Algebra and its Applications*, 548, pp. 95122
- [32] F. Grünbaum (2003), The Heisenberg inequality for the discrete Fourier transform. *Applied and Computational Harmonic Analysis*, 15, p. 163.
- [33] P. Barone (2008), A new transform for solving the noisy complex exponentials approximation problem. *Journal of Approximation Theory* 155, p. 1.
- [34] M. Shadlen, W. Newsome (1995), Is there a signal in the noise? *Current opinion in neurobiology* 5, p. 248.
- [35] T. Radüntz, J. Scouten, O. Hochmuth, B. Meffert (2015), EEG artifact elimination by extraction of ICA-component features using image processing algorithms. *J Neurosci Methods* 243, pp. 84-93.
- [36] G. Lu, J.-S. Brittain, P. Holland, J. Yianni, A. Green, et al. (2009), Removing ECG noise from surface EMG signals using adaptive filtering. *Neurosci Lett.* 462, pp. 14-19.
- [37] S. Strogatz (2000), From Kuramoto to Crawford: exploring the onset of synchronization in populations of coupled oscillators. *Physica D* 143, p. 1.
- [38] A. Arenas, A. Díaz-Guilera, J. Kurths, Y. Moreno, C. Zhou (2008), Synchronization in complex networks. *Physics Reports* 469, p. 93.
- [39] F. Hoppensteadt, E. Izhikevich (1999), Oscillatory Neurocomputers with Dynamic Connectivity. *Physical Rev. Lett.* 82, p. 2983.